Photoacoustics 22 (2021) 100257

Contents lists available at ScienceDirect

Photoacoustics

journal homepage: www.elsevier.com/locate/pacs

Laser induced thermoelastic contributions from windows to signal background in a photoacoustic cell

Lixian Liu [a,1], Huiting Huan [a,1], Xueshi Zhang [a], Le Zhang [a], Xiaopeng Shao [a,*], Andreas Mandelis [b], Lei Dong [a]

[a] School of Physics and Optoelectronic Engineering, Xidian University, Xi'an, 710071, China
[b] Center for Advanced Diffusion-Wave and Photoacoustic Technologies (CADIPT), Department of Mechanical and Industrial Engineering, University of Toronto, Toronto, ON, M5S 3G8, Canada

ARTICLE INFO

Keywords:
Photoacoustic cell
Thermoelasticity
Signal background
Green function

ABSTRACT

The existence of a signal baseline due to a variety of reasons in a photoacoustic (PA) gas measurement system is a common phenomenon. One major component is the absorption of optical windows in an enclosed PA cell. This work explores the relation between the background signal and the thermoelastic effect inside the windows by modelling the pressure and elastic wave field by means of a Green-function based method. The influence of laser incidence location, angle and radius is discussed based on a rigorous three-dimensional solid-to-fluid coupling model. The effects were theoretically demonstrated culminating in the determination of best (minimum background signal) performance using a collimated and expanded incident laser beam. The results were also validated through experiments.

1. Introduction

The photoacoustic cell is the key component in photoacoustic spectroscopy (PAS) systems used in trace gas detection. The performance of a PA cell in terms of its resonant frequency and Q-factor is of significant importance in enhancing the resolution in trace gas concentration measurements [1]. So far, many state-of-the-art researches demonstrated that the detection limit of PA spectroscopy can reach up to sub parts-per-trillion (ppt) level [2,3]. The growing number of reports in the field of trace gas detection by PAS makes the sensitivity of this technique promising for more in-field applications.

The huge progress made in gas detection PAS in recent years can generally be attributed to the improvement of the signal-to-noise (SNR) ratio of PA signals. One approach has been to develop more sensitive, sophisticated and miniaturized sensors inside the PA cell for the purpose of signal enhancement. Tomberg et al. used a cantilever - an extremely sensitive displacement sensing unit and a group of external reflectors to construct a PA cell and detect acetylene concentration. Sensitivity of a few tens of ppt level was attained [3,4]. Zheng et al. adopted quartz tuning forks to enhance PAS detection with Q-factors in the tens of thousands [5]. Xiong et al. developed a special optical grating that matched the resonant frequency of the detector crystal so as to amplify PA signals [2]. Other approaches adopted by many researchers are more straightforward. High power sources were adopted to increase the gas-absorbed energy. Karhu et al. introduced an amplified optical frequency comb and an optical parametric oscillator to test methane. The detectability floor was less than 100 ppb with about 0.1 W optical power [6]. A 1.4-W and 3.5-W laser source were respectively used by Yin et al. to measure hydrogen sulfide and nitrogen dioxide with ppb to sub-ppb detectability [7,8].

Instead of enhancing PA signals, some researchers have made efforts to sufficiently suppress background absorptions due to the optical windows, which also significantly improves the SNR in a PA cell. Brewster windows were used in many works [9,10] to minimize the laser energy loss at windows. González et al. reported an optical differential configuration to cancel coherent absorption from optical windows. The detection limit was thus improved by about 25 times [11]. Similarly, Saarela et al. used microphones to monitor the signal difference due to window absorption and made appropriate compensation for it [12]. Lassen *et al.* also implemented compensation by exciting a PA cell in its second-harmonic radial mode with microphone signals 180 degrees out-of-phase [13]. Liu et al. introduced an auxiliary

* Corresponding author.
E-mail addresses: xpshao@xidian.edu.cn (X. Shao), donglei@xidian.edu.cn (L. Dong).
[1] L.L. and H.H. made equal contribution with respect to this work.

https://doi.org/10.1016/j.pacs.2021.100257
Received 4 November 2020; Received in revised form 31 January 2021; Accepted 26 February 2021
Available online 2 March 2021

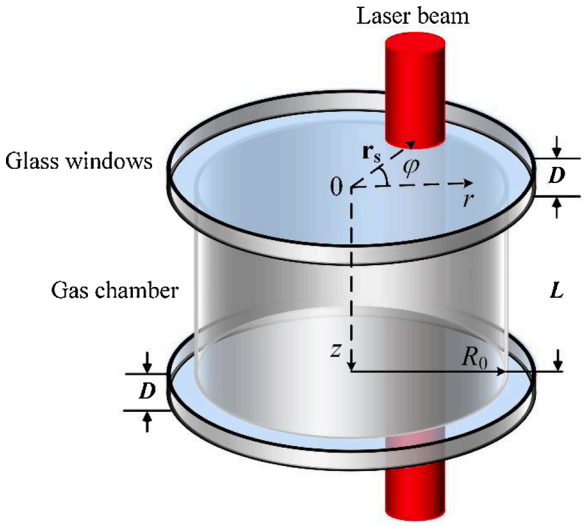

Fig. 1. Physical model for cylindrical PA cell with optical windows.

PA cell identical to the primary cell to perform differential measurements. The detection limit achieved was at ppm levels with merely a few tens of microwatts incoherent source [14,15]. In other reports, optical windows were even discarded and replaced with buffers [16, 17], which facilitates the so-called "open path detection" modality [18]. Such designs completely avoid window absorption, but the loss of optoacoustic energy confinement due to the open design significantly degrades the SNR.

In view of the foregoing design considerations, the following question arises: If the optical windows have to be retained in a PA cell, is it possible to minimize their optical absorption by adjusting the parameters of the incident beam? Before addressing this question, it is important to analyze how windows absorb laser power and contribute to the coherence noise background. Very recently, Cotterell et al. established a finite element model to study separately the absorption behavior of the windows and the target gas [19]. The theoretical Q-factor and the SNR was derived with respect to a PA cell based on the simulation result. However, their model cannot solve two problems: First, the spatial distribution of laser intensity which may affect the background baseline was not considered. Second, given that the glass window is a typical elastic solid, it is inaccurate to consider it as thermoviscous medium which should be a fluid property, thereby altogether neglecting its shear modulus. In this work, a detailed discussion on the effects of window absorption and the associated background noise is systematically presented by analyzing the pressure wave modes within the framework of thermoelastic theory. Optical beam parameters such as size, power distribution and incident location/angle are taken into account in the theoretical analysis. The influence of the glass-window-induced thermoelastic effect is considered along with the existence of solid-to-fluid interfaces in a cylindrical PA cell. Finally, experiments were conducted to validate the theoretical results.

2. Theoretical modelling

The photoacoustic effect was discovered by Bell in 1880 and its application to solids was first modeled by Rosencwaig and Gersho in 1976 in a gas-microphone system. The signal, simplified in one dimension, was interpreted by means of coupling between heat conduction and pressure-wave generation inside a hermetically sealed PA cell [20]. The performance and acoustic wave modes of PA cells has also been analyzed based on the Beer-Lambert law and theoretical acoustics [21–23]. However, the reported models of the window absorption have not been systematic and have neglected the influence of the laser beam parameters. In this article, we consider the PA signal induced only by the absorption of optical windows and explore the correlation between the incident laser beam parameters and the background signal. The effects of symmetric (axially concentric) and asymmetric (displaced from center) beam were also investigated.

We consider cylindrical PA cell filled with ideal zero-absorption gases such as nitrogen or other inert gases, as shown in Fig. 1. The incident laser beam passes through the cell and gives rise to the photoacoustic effect due to absorption by the two glass windows. For a modulated Gaussian laser beam going through an optical window, the spatial power distribution is

$$g(\mathbf{r},t)=\frac{Q_0}{\pi c^2 R_0^2}\exp\left[-\left(\frac{|\mathbf{r}-\mathbf{r}_s|^2}{c^2R_0^2}\right)-\beta z+i\omega t\right],0\le z\le D \tag{1}$$

where Q_0 is the original output power in W, β is the optical absorption coefficient of the glass window in m^{-1}, R_0 is the radius of the cylindrical cell and the two identical windows; c is an adjustable factor indicating the radius of divergence of the incident laser beam between the extreme cases of a point source ($c \to 0$) and full window surface illumination ($c \to 1$); $\mathbf{r}_s$ denotes the beam incidence location in the $z = 0$ plane and, therefore, $|\mathbf{r}-\mathbf{r}_s|^2 = r^2 + r_s^2 - 2rr_s\cos(\varphi-\varphi_s)$ denotes the Euclidean distance (displacement) between the observation and source locations. In practice, the optical windows for the PA cell are chosen such that they have very low absorption in the operating wavelength range, so that β is small enough to assume uniform power density distribution along its path through the windows. The laser induced temperature field T satisfies the heat conduction equation in cylindrical coordinates:

$$\frac{1}{r}\frac{\partial}{\partial r}\left(r\frac{\partial T}{\partial r}\right)+\frac{1}{r^2}\frac{\partial^2 T}{\partial\varphi^2}+\frac{\partial^2 T}{\partial z^2}-\frac{i\omega}{\alpha}T=-\frac{g(\mathbf{r},\omega)}{\kappa} \tag{2}$$

where κ and α represent the thermal conductivity and thermal diffusivity of the window, respectively. The temperature field should satisfy a zero flux condition on all surfaces of the enclosed window because heat exchange between glass and gases can be neglected at high modulation frequencies:

$$\left.\frac{\partial T}{\partial r}\right|_{r=R_0}=\left.\frac{\partial T}{\partial z}\right|_{z=0}=\left.\frac{\partial T}{\partial z}\right|_{z=D}=0 \tag{3a}$$

Cylindrical symmetry requires that a periodic condition in the azimuthal direction should be satisfied:

$$T(r,\varphi,z)=T(r,\varphi+2\pi,z) \tag{3b}$$

Eq. (2) with the boundary conditions of Eq. (3) can be conveniently solved using the Green function approach and Gauss's Theorem. Derivation details can be found elsewhere [24] which yield the following expression for the temperature field inside the glass window:

$$T(r,\varphi,z)=-\int_{V_D}\frac{Q_0}{\pi c^2R_0^2}\exp\left[-\frac{|\mathbf{r}'-\mathbf{r}_s|^2}{4c_2^2R_0^2}-\beta z'\right]G_T(r,\varphi,z\,|\,r',\varphi',z')dV'_0$$

$$=\frac{Q_0}{\kappa(\pi cR_0)^2}\sum_{n=0}^{\infty}\sum_{m=-\infty}^{\infty}\frac{\beta D[1-(-1)^n e^{-\beta D}]e^{im(\varphi-\varphi')}}{\Delta I_{mn}(\beta^2D^2+n^2\pi^2)(1+\delta_{n0})}\cos\left(\frac{n\pi z}{D}\right)\times INT_{mn}(r) \tag{4}$$

Here, G_T is the Green function for the temperature field (Eqs. (5.150) and (5.159) in Ref. [24]); δ_{n0} is the Kronecker delta, equal to unity only if $n = 0$. It is used to incorporate the dc (zero frequency) components in the cosine functions of Eq. (4); $INT_{mn}(r)$ denotes integration over the r-ϕ plane:

$$INT_{mn}(r) = \int_0^{2\pi} d\varphi \left\{ \int_0^{r} e^{-\frac{|\mathbf{r}-\mathbf{r}_s|^2}{4\sigma_0^2 R_0^2} - im(\varphi-\varphi')} [\Delta I_{mn} K_m(q_n r) - I_m(q_n r)\Delta K_{mn}] I_m(q_n r') r' dr' + \int_r^{R_0} e^{-\frac{|\mathbf{r}-\mathbf{r}_s|^2}{4\sigma_0^2 R_0^2} - im(\varphi-\varphi')} [\Delta I_{mn} K_m(q_n r') - I_m(q_n r')\Delta K_{mn}] I_m(q_n r) r' dr' \right\} \tag{5}$$

The other symbols in Eqs. (4) and (5) are defined as

$$q_n^2 = \frac{i\omega}{\alpha} + \left(\frac{n\pi}{D}\right)^2 \tag{6a}$$

$$\Delta I_{mn} = I_{m-1}(q_n R_0) + I_{m+1}(q_n R_0) \tag{6b}$$

$$\Delta K_{mn} = -K_{m-1}(q_n R_0) - K_{m+1}(q_n R_0) \tag{6c}$$

where I_m and K_m are modified Bessel functions of the first and second kind, respectively. The laser induced temperature field inside the glass window can be derived by combining Eqs. (4)–(6) and performing numerical integration. The temperature field further evolves into thermoelastic stress which can be denoted as [25]

$$\tau_{ii} = -3B_u \alpha_l \nabla_i T, i = r, \varphi, z \tag{7}$$

where B_u is the bulk modulus of the glass window, α_l is the linear thermal expansion coefficient, ∇_i denotes the gradient of T along the i-axis ($I = r$, ϕ or z), and the negative sign indicates that the stress is along the direction of the decreasing temperature field. The optical window glass is made by crystallized calcium fluoride and exhibits anisotropic elasticity with respect to different crystal symmetry and treatment temperatures [26]. However, the very weak absorption in the near-infrared region always results in infinitesimal strain in the glass which can still be treated as elastically isotropic [27]. In the elastic regime, the generalized Hooke's law depicts the stress-strain relation simply as proportional:

$$\tau_{ij} = \lambda \varepsilon_{kk} \delta_{ij} + 2\mu \varepsilon_{ij} \tag{8}$$

with λ and μ denote Lamé constants. Applying the balance of force and decomposing the displacement field into non-divergent and non-rotational components φ and $\boldsymbol{\psi}$, i.e. displacement field potentials, the elastic wave propagation can be represented as [28]

$$\nabla_i \left[\nabla^2 \phi + k_L^2 \phi - 3B_u \alpha_l T(r, \varphi, z)\right] + \nabla_i \times \left(\nabla^2 \boldsymbol{\psi} + k_T^2 \boldsymbol{\psi}\right) = \mathbf{0} \tag{9}$$

where φ and $\boldsymbol{\psi}$ are scalar and vector displacement potentials, respectively. k_L and k_T are longitudinal and transverse wave numbers in glass. Eq. (9) will evolve into four coupled equations satisfying predefined homogenous displacement and stress boundary conditions:

$$u_r(R_0, \varphi, z) = u_\varphi(R_0, \varphi, z) = u_z(R_0, \varphi, z) = 0 \tag{10a}$$

$$\boldsymbol{\tau}(r, \varphi, 0) = \boldsymbol{\tau}(r, \varphi, D) = \mathbf{0} \tag{10b}$$

Eq. (10a) denotes fixed radial conditions and Eq. (10b) indicates a stress-free condition for two horizontal surfaces. The normal displacement component u_z can be expressed by

$$u_z = \left[(\nabla \phi + \nabla \times \boldsymbol{\psi}) \cdot \mathbf{n}\right]|_{z=D \text{ or} 0} \tag{11}$$

where $\mathbf{n}$ denotes the normal unit vector along the z-direction.

The boundary value problem of Eqs. (9)–(11) usually does not have analytical solutions and only numerical methods can be applied. Driven by the normal displacement of the glass at the window-gas interfaces, the background pressure field of interest can be determined by solving the Helmholtz wave equation in the PA cell

$$\frac{1}{r}\frac{\partial}{\partial r}\left(r\frac{\partial p}{\partial r}\right) + \frac{1}{r^2}\frac{\partial^2 p}{\partial \varphi^2} + \frac{\partial^2 p}{\partial z^2} + k_0^2 p = 0 \tag{12}$$
$$0 \le r \le R_0, 0 \le \varphi \le 2\pi, 0 \le z \le L$$

Since we assumed no gas absorption in the chamber, no source term appears in Eq. (12). k_0 is the angular wave number in the gas. In the radial direction, the pressure field must be finite at the origin and total reflection is considered on the lateral wall:

$$|p(0, \varphi, z)| < +\infty \tag{13a}$$

$$\left.\frac{\partial p}{\partial r}\right|_{r=R_0} = 0 \tag{13b}$$

For the upper and lower horizontal surfaces, continuous velocity boundary conditions are imposed [29]:

$$\left.\frac{\partial p}{\partial z}\right|_{z=0} = \rho_0 \omega^2 u_{z1}(r, \varphi) \tag{13c}$$

$$\left.\frac{\partial p}{\partial z}\right|_{z=L} = \rho_0 \omega^2 u_{z2}(r, \varphi) \tag{13d}$$

where u_{z1} and u_{z2} denote the surface normal displacement at the two interfaces and can be determined by numerical calculation of Eqs. (9)–(11). The boundary value problem of Eqs. (12) and (13) can be solved using the Green function approach for the wave equation. Noting that Eq. (12) is analogous to Eq. (2), the Green function can be readily obtained by modifying the expression derived in Ref. [24]:

$$G_p(r, \varphi, z | r', \varphi', z') = \frac{1}{2L} \sum_{n=0}^{\infty} \sum_{m=-\infty}^{\infty} \frac{e^{im(\varphi-\varphi')}}{\Delta J_{mn}(1+\delta_{n0})} \cos\left(\frac{n\pi z}{L}\right) \cos\left(\frac{n\pi z'}{L}\right) \times \begin{cases} [Y_m(s_n r')\Delta J_{mn} - J_m(s_n r')\Delta Y_{mn}] J_m(s_n r), 0 < r \le r' \\ [Y_m(s_n r)\Delta J_{mn} - J_m(s_n r)\Delta Y_{mn}] J_m(s_n r'), r' \le r < R_0 \end{cases} \tag{14}$$

where

$$s_n^2 = k_0^2 - \left(\frac{n\pi}{L}\right)^2 \tag{15a}$$

$$\Delta J_{mn} = J_{m-1}(s_n R_0) - J_{m+1}(s_n R_0) \tag{15b}$$

$$\Delta Y_{mn} = Y_{m-1}(s_n R_0) - Y_{m+1}(s_n R_0) \tag{15c}$$

Here, J_m and Y_m are Bessel functions of the first and second kind of order m. δ_{n0} is defined in Eq. (4). Combining Eqs. (12) and (14) and applying Green's Theorem, the pressure wave field induced by window thermoelastic displacements can be determined

$$p(r, \varphi, z, \omega) = -\rho_0 \omega^2 \int_0^{R_0} \int_0^{2\pi} \left[G_p(z' = L) u_{z2}(r, \varphi) + G_p(z' = 0) u_{z1}(r, \varphi)\right] d\varphi' dr' \tag{16}$$

Eq. (16) can be calculated by performing a numerical double integration. The foregoing analysis connects the laser induced heating effect on glass in Eq. (4) with the surface displacement field in Eq. (11). The background pressure is calculated subject to the continuity boundary conditions denoted in Eqs. (13). In this manner, the model can account separately for background pressure due to thermoelastic effects in the cell windows distinct form the photoacoustic contribution to the cell gas pressure.

3. Beam profile simulations and discussion

3.1. Thermoelastic effects in cell windows

The thermoelastic behavior of glass windows was fist investigated by

Table 1
Typical properties of the window glass used in calculation.

Material	α, mm^2/s	κ, W/(m K)	α_b, K^{-1}	B_u, GPa	μ, GPa	ρ (density), kg/m^3
CaF_2	3.58	9.71	1.89×10^{-5}	82.7	33.8	3180

changing the optical parameters of the incident laser. An 8-mm-diameter, 3-mm-thick cylindrical glass window which has 0.2 m^{-1} absorption coefficient at the incident wavelength was modeled. The rest of the physical properties of window are shown in Table 1. Fig. 2 shows the results calculated using Eqs. (4), (9) and (11). The expanded beam has much smaller power density but more extended diffusion wave field. The existence of a temperature gradient further develops into thermoelastic vibration (oscillation) inside the window as depicted in Fig. 2(b). It is seen that the thermoelastic magnitude distribution coincides with the temperature field profile. The influence of beam size is obvious as the maximum displacement decreases with expanded beams, as shown in Fig. 2(c). Meanwhile if the incident beam is shifted away from the center, i.e. $|r_s|$ increases from zero, the displacement decreases almost exponentially as shown in the inset, only this change is not as effective as the change of beam size.

The explanation of this result is straightforward. The optical window, as an elastic circular plate, vibrates with fixed radial edge. The coaxial laser beam incidence has azimuthal symmetry and thus efficiently converts optical energy into nonradiative (photothermal) heating and subsequent thermoelastic expansion and oscillation. However, since the modulation frequency of the laser becomes much lower than the eigenfrequencies of the elastic modes in glass (corresponding to the eigenvalues of Eq. (9), e.g. 8.58 kHz, 15.19 kHz etc.), the thermoelastic effect is localized and decays rapidly as the observation point moves away from the illuminated area.

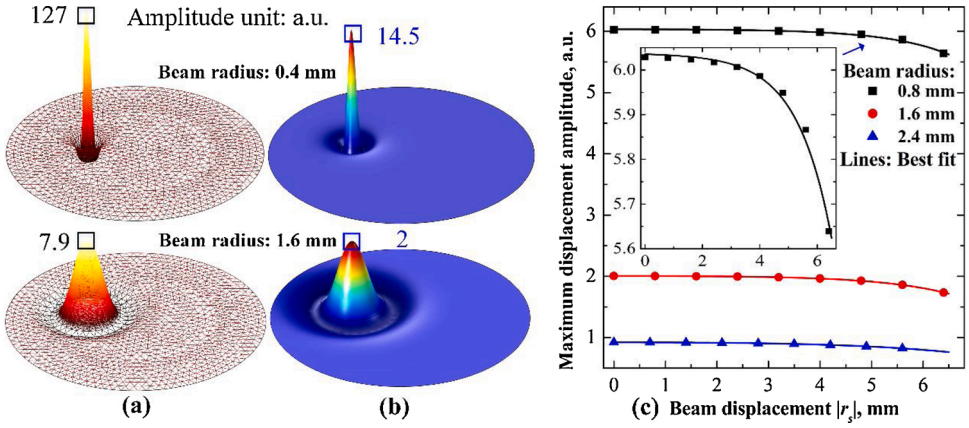

Fig. 2. Numerically calculated 3-D model: **(a)** Temperature field; **(b)** normal displacement field of glass-gas interface (the deformation magnitude does not reflect the real value); and **(c)** the maximum displacement amplitude as a function of beam displacement and beam size. The inset is a magnified curve of 0.8 mm beam size (modulation frequency f =715.3 Hz).

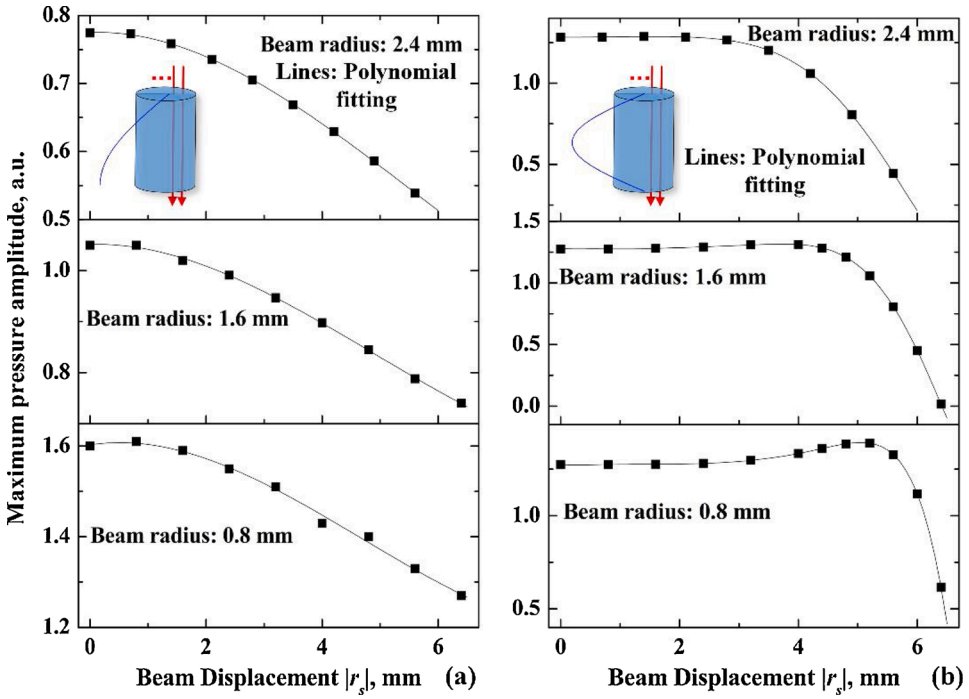

Fig. 3. Background signal dependence of beam displacement $|r_s|$ in the PA cell under symmetric illumination: **(a)** fundamental mode (f =715.3 Hz); **(b)** second-order longitudinal mode (f =1430.6 Hz).

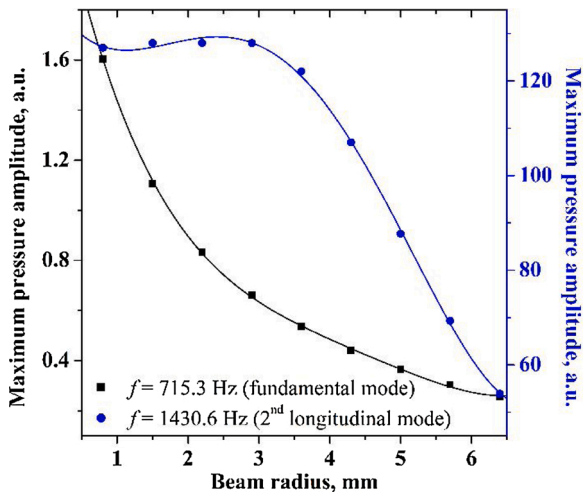

Fig. 4. Background signal dependence on beam radius under symmetric illumination (displacement $r_s = 0$).

3.2. Background pressure field with symmetric illumination

An analysis of how the thermoelastic oscillation in the cell windows couples into the PA cell was carried out considering the coupling conditions in Eqs. (13a–d). If the incident laser beam is collimated along the axis of the cylindrical PA cell, the oscillation features with respect to the two optical windows are identical. Such cases are named "symmetric illumination". As shown in Fig. 3, the window-generated background pressure is lowest at the boundary where the incident laser beam exhibits the largest displacement, impinging close to the boundary. The second-longitudinal mode was also analyzed because it is frequently used in practical PA gas detection applications [1]. There exists an obvious maximum for the second-order longitudinal mode with respect to small beam size.

The beam size effect is shown in Fig. 4 for both fundamental and second-order modes. The maximum pressure amplitude decreases monotonically for the fundamental mode when the beam expands. This feature suggests that the thermoelastic response amplitude is mainly responsible for the background signal. However, there also exists a non-monotonic broad maximum in the second-order mode behavior of the beam around radius <3 mm, which implies the background pressure does not depend solely on the vibration amplitude of each window, but is also affected by the longitudinal acoustic mode symmetry in the PA cell.

A qualitative physical explanation is as follows: the background acoustic signal is affected by two factors: The first is the amplitude of the thermoelastic response (the fraction of non-radiative energy being coupled into the cell) at the solid-gas interface. This effect is closely related to the location of incidence and the beam size as shown in Fig. 2. It constitutes the main background in the fundamental thermoelastic excitation mode, as higher optical power density and smaller displacement produce higher signal (Fig. 3(a)). The other factor is the thermoelastic oscillation symmetry on the two optical windows. This effect becomes obvious for the second-order longitudinal mode, the pressure field of which is in-phase on both sides of the cell. If the incident laser beam results in the same oscillation pattern on both windows, the oscillation of the windows produces in-phase translational motion of the gas in the cell which does not contribute to the background. This explains the fact that the background signal remains steady for small displacements even if the window oscillation is strong, as shown in Figs. 3(b) and 4 .

3.3. Background pressure field with asymmetric illumination

The foregoing analysis suggests that the background signal can be minimized if the beam is expanded and impinges on the window at large displacement from the center axis of symmetry. In practice, it is quite difficult to maintain two identical incident coordinate locations with respect to beam entrance and exit windows. The word "asymmetric" denotes the fact that the thermoelastic oscillations of two windows differ. The asymmetric illumination model considers two displaced beam spots on the two windows independently, a configuration which corresponds to the case of oblique incidence. As shown in

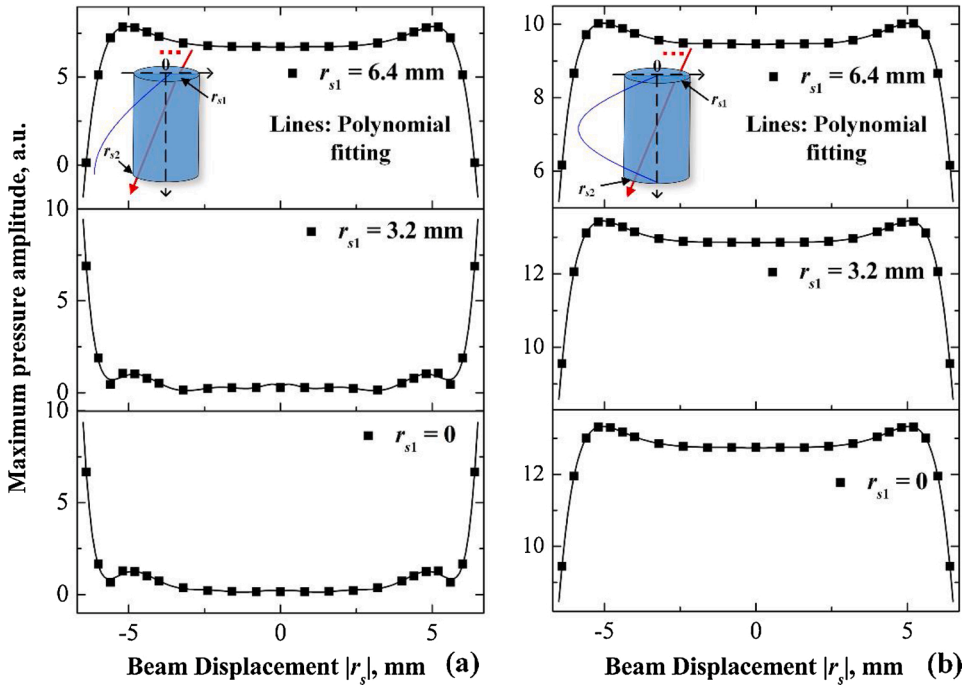

Fig. 5. Background signal dependence on beam displacement in the case of oblique incidence (r_{s1} and r_{s2} represent the displacement of the incident and exit beam, respectively): **(a)** fundamental mode (f =715.3 Hz); **(b)** second-order longitudinal mode (f =1430.6 Hz); beam radius: 0.8 mm.

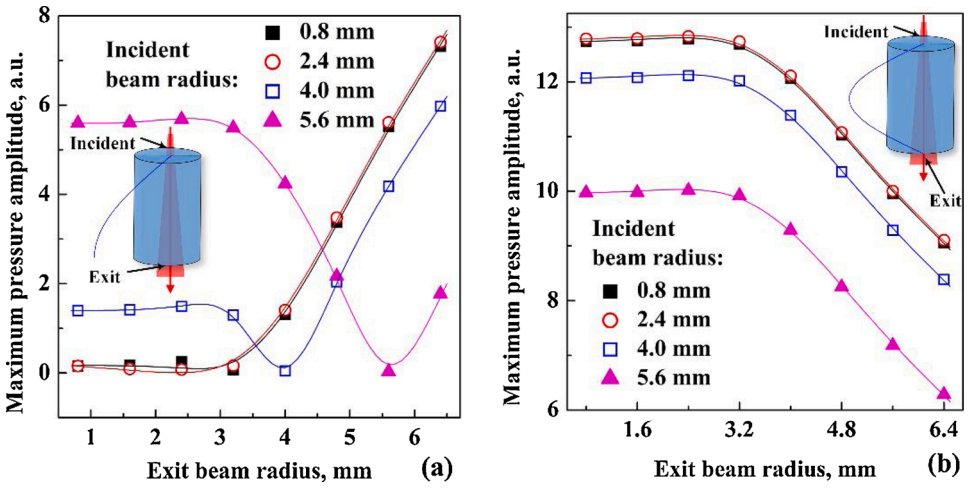

Fig. 6. The background signal oscillation as a result of beam expansion (centered illumination): **(a)** fundamental mode (f =715.3 Hz); **(b)** second-order longitudinal mode (f =1430.6 Hz).

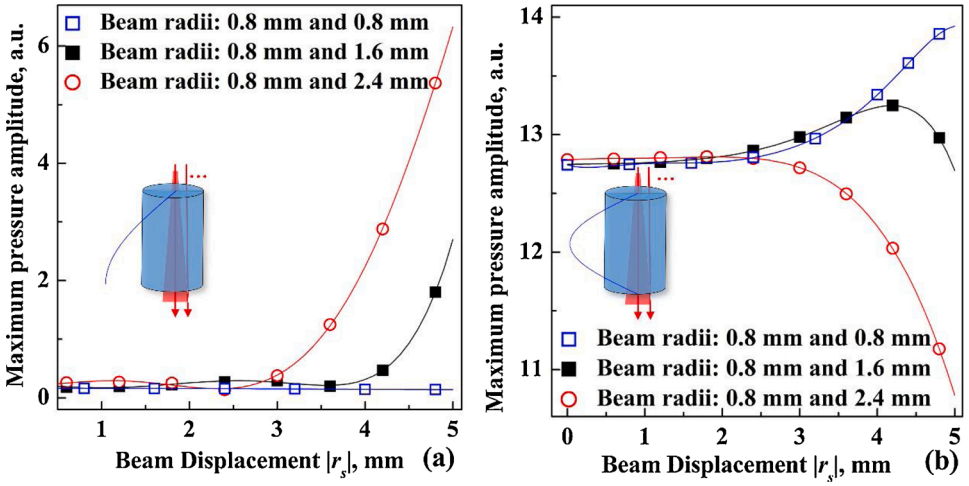

Fig. 7. The background pressure dependence on the displacement of an axially incident and co-axially divergent beam: **(a)** fundamental mode (f =715.3 Hz); **(b)** second-order longitudinal mode (f =1430.6 Hz).

Fig. 5, the maximum pressure for the fundamental mode depends on the beam incidence locations of both windows. If the incident beam is close to the boundary, minimal background signal can be obtained only if it exits close to the boundary too (i.e. at a large incidence angle). Normally, both incident and exiting beams should be located near the axis of the cylinder. The performance of the second-order longitudinal mode, shown in Fig. 5(b), is similar to that in Fig. 3(b) with an obvious maximum around $r_{s2} = \pm 5$ mm. The background signal is minimized if both entrance and exit locations are near the boundary.

In practical PA spectroscopic applications, beam divergence is a common phenomenon in diode lasers, a fact that further alters the thermoelastic behavior of the entrance and exit optical windows. The effect of beam expansion was also analyzed with the foregoing model by adjusting the parameter c with respect to the two windows. As shown in Fig. 6 for the fundamental mode, when one of the beam radii is small enough (e.g. smaller than half the radius of the window), the background pressure increases when the other beam radius increases (black-solid squares and red-hollow circles). Otherwise, if the beam radius on one side is larger than half the window radius, there exists a minimum point which corresponds to the case of the aforementioned non-divergent (equal radii) illumination. This result suggests the importance of maintaining identical spot sizes through precise collimation on both windows for the purpose of suppressing the background in the fundamental mode. For the second-order mode, the background dependence on beam radii is plotted in Fig. 6(b). Given that the divergent beam produces asymmetric thermoelastic oscillations in both windows, the window oscillation amplitude dominates the pressure field again. The minimal background signal is obtained when the beam is expanded to its greatest extent (close to the window size).

In the more general case, the divergent beam enters parallel to the cylinder axis and becomes displaced from the center inside the cell. The background pressure as a function of displacement at several divergence angles is plotted in Fig. 7. The largely displaced divergent beam has an obvious influence on the background fundamental mode pressure: the maximum pressure steeply increases with increased displacement. For the second-order mode, the divergent beam only left-shifts the r_s value, thereby giving rise to a maximal pressure point, as shown in Fig. 7(b) with an r_s dependence similar to that in Fig. 3(b).

4. Experimental validation

The theoretical calculations and discussion with respect to the photothermoelastic effect in optical windows were further validated with

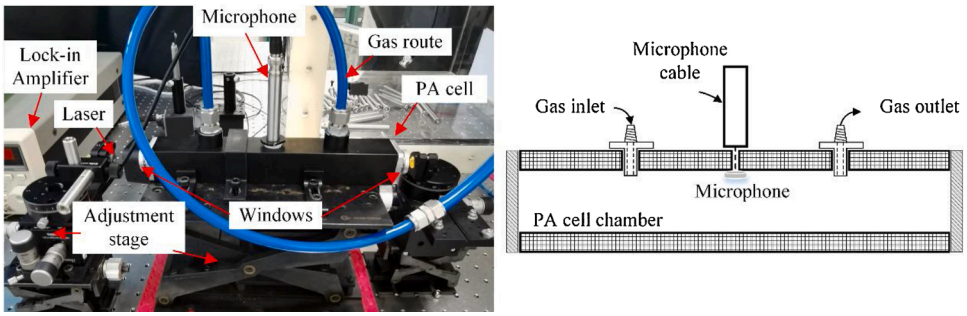

Fig. 8. The gas detection PA experimental setup (left) and the cross-section of the PA cell (right), the microphone was installed at the center, near the internal boundary.

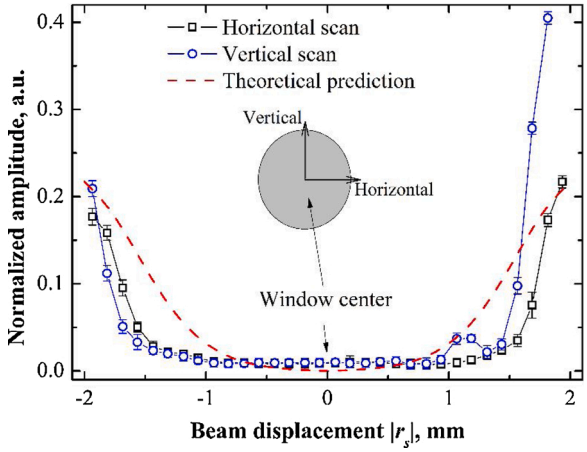

Fig. 9. Experimental validation of window absorption with displaced incident laser beam. Incident beam-size: 0.3 mm, exiting beam-size: 2.8 mm; The experimental results are normalized to the corresponding theory.

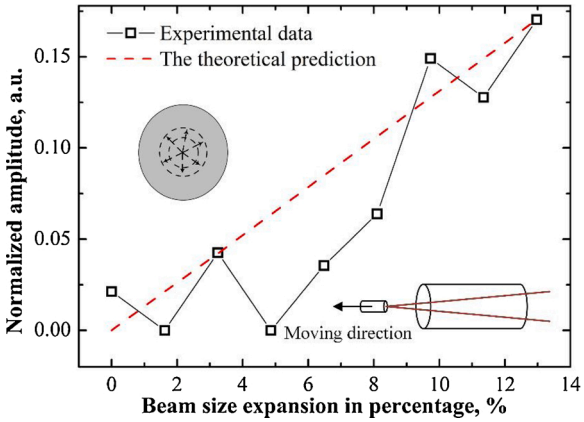

Fig. 10. Effect of incident beam size on PA cell window at the center of cylindrical symmetry. Beam radii: 0.3 mm and 2.8 mm for the incident and exiting beam, respectively; The experimental results are normalized to the corresponding theory.

experiments. The PA experimental setup is shown in Fig. 8. A cylindrical aluminum-alloy PA cell of 8-mm diameter and 240-mm length with polished internal surfaces was used. The cell was filled with nitrogen gas, a good optical non-absorber in the near infrared regime, to study the effect of window absorption under ambient pressure. The optical windows were made of 3-mm-thick calcium fluoride glass which has good transparency to the incident 1.65 μm laser beam. Nevertheless, about 5% optical energy was reflected, while 0.12 % energy was absorbed by the two glass windows and subsequently contributed to the appearance of a background signal. The cell was operating at its second-order longitudinal mode (about 1410 Hz) so that the maximum pressure occurred at the half-wavelength where a capacitor microphone MP-201, BSWA Tech®, China, Diameter: 1/2 in. Sensitivity: 50 mV/Pa, Range: 6.3 Hz to 20 kHz) was installed to measure the PA signal.

The incident laser beam axis was adjusted parallel to the cylinder axis. The measured radii of the incident and exiting beam were 0.3 mm and 2.8 mm, respectively. The divergence of the laser beam was known from the laser specifications. Two alignment cards with crosshairs at the center were also placed in front of the windows to make sure the concentric beam spot was unchanged during the vertical and horizontal scans. The theory was modified by adjusting the beam-size parameters (c and r_s in Eq. (1)) accordingly. Fig. 9shows the experimental and theoretical normalized results of the background pressure distribution obtained by scanning the incidence location of the beam horizontally and vertically. In agreement with the theoretical prediction trends, a larger background signal was captured when the laser deviated from the center, nevertheless, there still existed a discrepancy between theoretical prediction and the experimental data in Fig. 9. This is because the theory only considers ideal thermoelastic and coupling conditions at the windows and ignores signal baseline. The last two points in the vertical scan shows accidentally high amplitude, which should be the result of beam misalignment and the scattering. The actual background signal obtained by the lock-in may also be affected by external noise and the microphone itself.

Table 2
Summary of the background signal property in a cylindrical PA cell.

Photoacoustic modes	Property	Influence of optical parameters on background	Recommendations
Fundamental longitudinal mode	a) Asymmetric mode b) Maximum pressure near either side of the cell	a) Sensitive to beam size b) Sensitive to divergence of beam c) Sensitive to displacement if the incident beam is divergent	a) Expanded incident beam b) Equalized beam size on both windows c) Avoidance of off-axis illumination
Second-order longitudinal mode	a) Symmetric mode b) Maximum pressure at half length of the cell c) Larger pressure amplitude than the fundamental mode	a) Sensitive to beam size b) Sensitive to beam divergence c) Insensitive to moderate displacements in all cases	a) Expanded incident beam b) Avoidance of large displacements away from center axis

In the next experiment, the incident laser beam was displaced away from the front window with its size diameter increased due to divergence, as depicted in the insets of Fig. 10. The contribution from subtle change of beam size in the background signal was considered. As shown in Fig. 10, a subtle increasing pattern of PA signal was obtained as the beam expanded, which is consistent with the theoretical trends.

The following conclusions for minimizing the background signal due to glass window absorption can be garnered from Table 2: The fundamental PA cell mode has lower amplitude background signal, but it is also less sensitive to the actual PA signal from absorbing gases and the detector should only be fixed at one end of the cell, a configuration seldom used in practice. For both the fundamental and 2nd order longitudinal modes inside the cell, an expanded incident beam can help decrease the window thermoelastic oscillation amplitude and thus suppress the background signal. Although the pressure field decreases rapidly when the laser beam is located near the wall, this situation is precarious and should be avoided since the scattered or stray light can be absorbed by the window surface and produce a large background signal.

5. Conclusions

In this study, a large portion of the background signal in PA spectroscopy applications has been shown to be due to the absorption of the optical windows of the PA cell. The coupling between the thermoelastic effect in the windows and the pressure wave inside the PA cell was established theoretically and experimentally. Significant conclusions obtained from the study were: 1) The thermoelastic effect due to laser absorption in optical windows contributes to the background/spurious signal in a PA gas cell which is dependent of incident laser parameters in terms of beam size and incident displacement; 2) An expanded beam size being kept identical on both windows can help minimize the background signal due to laser beam absorption and non-radiative thermal generation leading to thermoelastic oscillations. In practice, this means strict collimation of the incident beam. 3) Large displacement from PA cell axis should be avoided.

Declaration of Competing Interest

The authors declare that there are no conflicts of interest.

Acknowledgements

L.L. and H.H. are grateful to the National Natural Science Foundation of China with Grant No. 61805187, 61801358. This work was also supported by the Natural Science Foundation of Shaanxi Province with Grant No. 2019JQ-651 and 2020JQ-293. L.L. acknowledges the China Postdoctoral Science Foundation under Grant No. 2019M653546. A.M. acknowledges the support of the Natural Sciences and Engineering Research Council of Canada (NSERC) for a Discovery grant and the support of the Canada Research Chairs program.

References

[1] A. Miklós, P. Hess, Z. Bozóki, Application of acoustic resonators in photoacoustic trace gas analysis and metrology, Rev. Sci. Instrum. 72 (2001) 1937.
[2] L. Xiong, W. Bai, F. Chen, et al., Photoacoustic trace detection of gases at the parts-per-quadrillion level with a moving optical grating, Proc. Natl. Acad. Sci. U. S. A. 114 (28) (2017) 7246.
[3] T. Tomberg, M. Vainio, T. Hieta, et al., Sub-parts-per-trillion level sensitivity in trace gas detection by cantilever-enhanced photo-acoustic spectroscopy, Sci. Rep. 8 (2018) 1848.
[4] T. Tomberg, M. Vainio, T. Hieta, et al., Cavity-enhanced cantilever-enhanced photo-acoustic spectroscopy, Analyst 144 (2019) 2291.
[5] H. Zheng, Y. Liu, B. Liu, et al., Quartz-enhanced photoacoustic spectroscopy employing pilot line manufactured custom tuning forks, Photoacoustics 17 (2020) 100158.
[6] J. Karhu, T. Tomberg, F.S. Vieira, et al., Broadband photoacoustic spectroscopy of $^{14}CH_4$ with a high-power mid-infrared optical frequency comb, Opt. Lett. 44 (5) (2019) 1142.
[7] X. Yin, L. Dong, H. Wu, et al., Ppb-level H_2S detection for SF_6 decomposition based on a fiber-amplified telecommunication diode laser and a background-gas-induced high-Q photoacoustic cell, Appl. Phys. Lett. 111 (2017), 031109.
[8] X. Yin, L. Dong, H. Wu, et al., Sub-ppb nitrogen dioxide detection with a large linear dynamic range by use of a differential photoacoustic cell and a 3.5 W blue multimode diode laser, Sens. Actuators B-Chem. 247 (2017) 329.
[9] F.G.C. Bijnen, J. Reuss, F.J.M. Harren, Geometrical optimization of a longitudinal resonant photoacoustic cell for sensitive and fast trace gas detection, Rev. Sci. Instrum. 67 (8) (1996) 2914.
[10] A.L. Ulasevich, A.V. Gorelik, A.A. Kouzmouk, et al., A compact resonant Π-shaped photoacoustic cell with low window background for gas sensing, Appl. Phys. B 117 (2) (2014) 549.
[11] M. González, G. Santiago, V. Slezak, et al., Novel optical method for background reduction in resonant photoacoustics, Rev. Sci. Instrum. 78 (2007), 084903.
[12] J. Saarela, T. Sorvajärvi, T. Laurila, et al., Phase-sensitive method for background-compensate photoacoustic detection of NO_2 using high-power LEDs, Opt. Express 19 (2011) A725.
[13] M. Lassen, A. Brusch, D. Balslev-Harder, et al., Phase-sensitive noise suppression in a photoacoustic sensor based on acoustic circular membrane modes, Appl. Opt. 54 (13) (2015) D38.
[14] L. Liu, A. Mandelis, H. Huan, et al., Step-scan T cell-based differential Fourier transform infrared photoacoustic spectroscopy (DFTIR-PAS) for detection of ambient air contaminants, Appl. Phys. B 122 (10) (2016) 268.
[15] L. Liu, A. Mandelis, H. Huan, et al., Step-scan differential Fourier transform infrared photoacoustic spectroscopy (DFTIR-PAS): a spectral deconvolution method for weak absorber detection in the presence of strongly overlapping background absorptions, Opt. Lett. 42 (7) (2017) 1424.
[16] T. Starecki, A. Geras, Improved open photoacoustic Helmholtz cell, Int. J. Thermophys. 35 (2014) 2023.
[17] S.A.S. El-Busaidy, B. Baumann, M. Wolf, et al., Modelling of open photoacoustic resonators, Photoacoustics 18 (2020) 100161.
[18] Z. Bozóki, A. Szabó, Á. Mohácsi, et al., A fully opened photoacoustic resonator based system for fast response gas concentration measurements, Sens. Actuators B-Chem. 147 (2010) 206–212.
[19] M.I. Cotterell, G.P. Ward, A.P. Hibbins, et al., Optimizing the performance of aerosol photoacoustic cells using a finite element model. Part 1: method validation and application to single-resonator multipass cells, Aerosol Sci. Technol. 53 (10) (2019) 1107.
[20] A. Rosencwaig, A. Gersho, Theory of the photoacoustic effect with solids, J. Appl. Phys. 47 (1976) 64.
[21] A. Rosencwaig, Photoacoustics and Photoacoustic Spectroscopy, Wiley-Interscience, New York, 1980, pp. 26–41.
[22] Y. Pao, Optoacoustic Spectroscopy and Detection, Academic Press, New York, 1977, pp. 47–62.
[23] P. Hess, Photoacoustic, photothermal and photochemical processes in gases, in: Topics in Current Physics, Vol. 46, Springer-Verlag, Heidelberg, 1989, pp. 85–121.
[24] A. Mandelis, Diffusion Wave Fields: Mathematical Methods and Green Functions, Springer, New York, 2001, pp. 359–370.
[25] R. White, Generation of elastic waves by transient surface heating, J. Appl. Phys. 34 (1963) 3559.
[26] K. Shinozaki, T. Honma, K. Oh-ishi, et al., Morphology of CaF_2 nanocrystals and elastic properties in transparent oxyfluoride crystallized glasses, Opt. Mater. 33 (2011) 1350–1356.
[27] F. Fedorov, Theory of Elastic Waves in Crystals (translated from Russian by J. Bradley), Springer, New York, 1968, pp. 85–117.
[28] J. Miklowitz, The Theory of Elastic Waves and Waveguides, North Holland, Amsterdam, 1980, pp. 38–46.
[29] H. Huan, A. Mandelis, B. Lashkari, et al., Frequency-domain laser ultrasound (FDLU) non-destructive evaluation of stress–strain behavior in an aluminum alloy, Int. J. Thermophys. 38 (2017) 62.

Lixian Liu received her B.S. degree of electronic science and technology and doctorate in optical engineering from the University of Electronic Science and Technology of China, in 2012 and 2017, respectively. She is now a full-time lecturer in the School of Physics and Optoelectronic Engineering, Xidian University. Her research field is photoacoustic and optical spectroscopy technologies.

Huiting Huan received his B.S. and Ph.D degrees from the University of Electronic Science and Technology of China in 2012 and 2017, respectively. He is now a researcher with the School of Mechano-Electronic Engineering, Xidian University. His main research field includes acoustics, electromagnetic and thermal radiometric non-destructive testing.

Xueshi Zhang is a graduate student at the School of Physics and Optoelectronic Engineering, Xidian University. He focuses on the high sensitivity trace gas detection technology.

Le Zhang is a Ph.D. student at the School of Physics and Optoelectronic Engineering, Xidian University. His research interests include photoacoustic spectroscopy and its application to trace gas detection.

Xiaopeng Shao received his Ph.D degree from Xidian University in 2005. He is a professor at the School of Physics and Optoelectronic Engineering, Xidian University. His research focuses on computational imaging, optical sensing and signal processing.

Andreas Mandelis received his B.S. degree in physics from Yale University, New Haven, CT, USA in 1974, followed by M. A., M.S.E., and Ph.D degrees in applied physics and materials science from Princeton University, Princeton, NJ, USA in 1976, 1977 and 1979, respectively. He is a Full Professor of mechanical and industrial engineering; electrical and computer engineering; and the Institute of Biomaterials and Biomedical Engineering, University of Toronto, Toronto, ON, Canada. He is the Director of the Center for Advanced Diffusion-Wave and Photoacoustic Technologies (CADIPT), Toronto. He is an author and coauthor of more than 410 scientific papers in refereed journals and 190 scientific and technical proceedings papers. He is the Editor-in-Chief of the Springer Nature International Journal of Thermophysics, and an Editor of the Journal of Biomedical Optics and the Journal of Applied Physics.

Lei Dong received his Master degree from Xidian University. He is a senior engineer at the School of Physics and Optoelectronic Engineering, Xidian University. His research focuses on computer vision, parallel computing, digital image processing.